The effect of solid boundaries on pore shrinkage in Stokes flow

By DARREN CROWDY AND LAURENT DUCHEMIN

Department of Mathematics, Imperial College of Science, Technology and Medicine, 180 Queen's Gate, London, SW7 2AZ, UK

Department of Applied Mathematics and Theoretical Physics, Centre for Mathematical Sciences, Wilberforce Road, Cambridge, CB3 0WA, UK

(Received 10 March 2004 and in revised form 25 January 2005)

Motivated by the viscous sintering of amorphous materials in the presence of a distribution of rigid platelet inclusions added to increase the strength of the final sintered medium, a simple model for the shrinkage of compressible pores close to a wall in Stokes flow is proposed. The model assumes that the pore remains elliptical/ellipsoidal in shape at all times. The model is expected to be valid provided the pore is not too far from spherical and not too close to the wall. It relies on a separation of the flow into 'inner' and 'outer' problems. The inner problem is to assume that the ellipsoid evolves in a linear ambient flow given by the first two terms in a local expansion of an outer flow produced by the image singularity distribution of a point-sink near a planar no-slip boundary. The focus of the present paper is to test the viability of the model in the planar case. Using a spectral method based on analytic functions and conformal mappings, the results of a full numerical simulation are compared with the predictions of the planar model. The effects of the proximity of the pore to the wall, the anisotropy in the pore shape and its relative orientation to the wall are all examined. It is observed that, as they shrink, pores drift towards the wall becoming elongated in the direction perpendicular to the wall.

1. Introduction

Viscous sintering is a process in which a granular compact or matrix of particles (e.g. metal or glass) is raised to a sufficiently high temperature that the individual particles become mobile and release surface energy in such a way as to produce inter-particulate bonds (Brinker & Scherer 1990). At the start of a sinter process, any two matrix particles which are initially touching develop a thin neck which, as time evolves, grows in size to form a more developed bond. As the necks grow in size, the sinter body densifies and any enclosed pores between particles eventually close up. The macroscopic material properties of the compact at the end of the sinter process depend heavily on the degree of densification. In industrial application, it is important to be able to obtain accurate estimates of the time taken for pores to close (or reduce to a sufficiently small size) within any given initial sinter body in order that industrial sinter times are optimized without compromising the macroscopic properties of the final densified material.

In an effort to increase the strength of a final densified sinter body, one procedure that is used is to lace the initial sinter compact with a distribution of rigid nondensifying platelets. These inclusions do not densify when the compact is sintered,

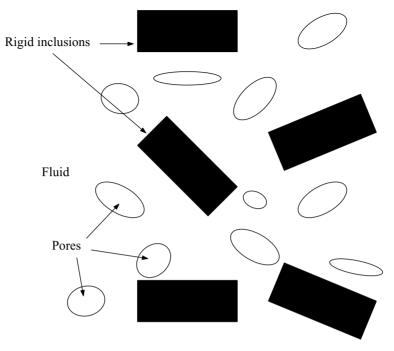


FIGURE 1. Viscous sintering in the presence of rigid inclusions. The pores close up under the effects of surface tension in a very viscous fluid also containing a distribution of rigid platelet inclusions added to strengthen the final densified sinter body.

rather, the surrounding sinter matrix densifies around any such inclusions. This naturally leads to sinter bodies consisting of pores that close up, under the effects of surface tension, in the vicinity of no-slip surfaces associated with the rigid platelets. Figure 1 shows a schematic. Boccaccini & Conradt (2001) have found experimentally that, while the addition of the platelets can lead to improved macroscopic properties of the final sinter body, the very presence of the platelets can impede the densification process, the pores taking much longer to disappear. The basic fluid dynamical problem considered in this paper has been motivated by this physical situation.

A natural first step in gaining a theoretical understanding of viscous sintering is to study a planar model. Much work has been done on this problem over the last fifteen years. From a numerical viewpoint, Kuiken (1990) performed some early studies of planar viscous sintering using boundary-element methods. This work was later extended by Van de Vorst (1993). Theoretical interest in the planar problem was revived when Hopper (1990) (see also Hopper 1991) observed that various 'unit problems' could be solved, in exact mathematical form, using complex variable methods. This includes the problem of the coalescence of two equal cylindrical particles. This has led to many new theoretical results including the coalescence of multiple particles in doubly connected configurations enclosing shrinking pores (Richardson 2000; Crowdy 2003a), exact solutions for the evolution of bubbles in Stokes flows (Tanveer & Vasconcelos 1995; Antanovskii 1994; Crowdy 2003b) as well as models, based upon these exact solutions, for the late stages of viscous sintering (Crowdy 2004).

While models of viscous sintering with rigid inclusions have been attempted in the past (see, for example, Scherer 1987) such models are, to a large extent, phenomenological. We have not found any studies in the literature which consider the problem of

pore shrinkage in Stokes flow with walls using detailed resolution of the free-surface evolution and the associated flow fields. For this reason, even before devising a model which incorporates the effects of contact lines between a pore interface and the no-slip surface on a rigid platelet, it seems appropriate to study the simple question of how the presence of a nearby wall can affect the time taken for a single pore to shrink to zero area when evolving purely under the effects of surface tension. This issue is investigated here. In the planar case, Hopper (1991) finds that an isolated circular pore of unit radius evolving purely under the effects of surface tension closes up in time $2\mu/\sigma$ where μ is the viscosity of the fluid and σ is the surface tension. He also investigated the shrinkage of elliptical and hypotrochoidal pores. Here, as a simple 'unit problem', we examine quantitively how this shrinkage time of a single pore is affected by the presence of a no-slip surface (supposed to model the effect of a nearby rigid platelet).

The aim of this paper is to present a simple analytical model of the shrinkage of a two- or three-dimensional pore in the presence of a wall. The model will be referred to as the 'ellipsoidal-pore' model. In the planar case, it reduces to an 'elliptical-pore' model. The model is based on an extension of ideas originally presented by Crowdy (2004) where the shrinkage of a general assembly of interacting pores in late-stage planar viscous sintering is considered. The idea there is to assume that each pore is elliptical in shape and thus completely characterized by the five parameters associated with the coordinates of its centroid position, its area and eccentricity and its orientation angle. Any given elliptical pore is then taken to be evolving in an 'outer' flow field generated by a distribution of irrotational point-sinks at the centroids of all other pores and with strengths equal to the rates-of-change of area of those pores. This outer flow field can be written down exactly. By expanding this outer flow field to linear order in the vicinity of the given pore, the 'inner' problem of a compressible elliptical pore evolving in an ambient linear straining flow can also be solved exactly, the governing equations having been presented in Crowdy (2003b).

It is worth mentioning that the basic idea of the elliptical-pore model for interacting pores presented in Crowdy (2004) was inspired by similar models of interacting vortical regions based on the 'elliptical-vortex approximation' (Melander, Zabusky & Styczek 1986; Saffman 1992) in the theory of vortex dynamics. The elliptical vortex approximation is to assume that all interacting vortices are ellipses evolving in a time-dependent strain field produced by the other elliptical patches. Such models are predicated on the fact that the Euler equations are such that elliptical vortex patches remain elliptical when placed in an ambient irrotational straining or shear flow. In the same way, the 'elliptical-pore' model presented in Crowdy (2004) is similarly predicated on the fact that the Stokes equations are such that compressible elliptical bubbles with surface tension also remain elliptical when placed in an ambient linear straining or shear flow (Crowdy 2003b).

The proper manner in which to test the viability of our ellipsoidal-pore model convincingly is to compare the predictions given by the model with numerical boundary integral simulations of the full three-dimensional system. Such simulations, while possible, are computationally demanding: indeed, in Pozrikidis (2000, 2003) the numerical difficulties associated with computing the pressure in compressible bubbles in three-dimensional Stokes flows have been discussed (special methods are required to negotiate the presence of hyper-singular integrals involved in computing the bubble pressure). Yet, our model has not even been tested in the planar case and it seems a sensible idea to examine this first. This is the subject of the present paper.

On this matter, it is worth remarking that the problem of two-dimensional Stokes flows involving both a free surface with surface tension and a solid no-slip boundary

have been studied previously using numerical methods (e.g. Pozrikidis 1988, 1992). The numerical method based on analytic functions and conformal mappings devised here is not commonly employed in the context of Stokes flows, yet their application to the mathematically similar problem of plane elasticity is more widespread (Mikhlin 1957). Greengard, Kropinski & Mayo (1996) discuss the two approaches. Here we find that the spectral method we employ leads to an appealing numerical formulation of the problem at hand, allowing effective calculation of pore shrinkage even for pores that are very close to the wall.

The layout of the paper is as follows. In §2, the idea underlying the ellipsoidal-pore model is presented. In §3, a full numerical simulation of the problem in the planar case is given. The results of these simulations are presented in §3 whereas, in §4, the equations of the elliptical-pore model are derived by combining ideas from singularity theory with known exact solutions for compressible ellipses. This model helps to provide some theoretical insight into the qualitative features observed in the numerical simulations and also provides good quantitative agreement with the numerics.

2. The elliptical/ellipsoidal-pore model

In this section, the ellipsoidal-pore model of a compressible pore shrinking near a wall will be described. The model is to assume that the pore remains ellipsoidal in shape at all times and will thus be completely characterized by its centroid position and a symmetric positive-definite second-rank tensor whose eigenvalues give the square semi-axes of the ellipsoid. Owing to the effects of surface tension, the tendency is for the pore to shrink. Since there are no net forces on the pore then, provided the pore is not too far from spherical, to leading order the shrinking pore should be well-modelled by a point sink positioned at the centroid of the pore and with strength equal to the rate-of-change of its volume (we note in passing that pores that are far from spherical may be better modelled by more general image systems such as a line distribution of image singularities as in Chwang & Wu 1975). Provided the pore is not too close to the wall, it is taken that the pore is sitting in an 'outer' flow field given by the image distribution associated with such a point sink placed near a wall. This image singularity distribution is associated with the fact that the no-slip boundary condition must be satisfied on the wall. The subsequent evolution of the ellipsoidal pore is then assumed to be given by the solution of an 'inner' problem consisting of an ellipsoidal pore evolving in a linear ambient straining flow obtained by locally expanding this outer flow field to linear order about the centroid of the pore. A schematic is shown in figure 2.

Having described the model, the solutions of both the outer and inner problems are required. Consider first the outer problem. Blake & Chwang (1974) have written down a closed-form solution for the image distribution associated with a point sink sitting near a stationary no-slip plane boundary in the three-dimensional case. This solution provides the requisite outer flow in the model.

The inner problem is more challenging. It is important to note that, in the three-dimensional case, it has not yet been shown mathematically that a compressible constant-pressure ellipsoidal bubble with non-zero surface tension remains ellipsoidal if placed in a linear far-field straining flow. Indeed, the result may not be true. However, the analogous result is true in two-dimensions: a compressible elliptical bubble remains elliptical under quasi-steady evolution in an ambient strain and/or shear flow. The governing equations are given in Crowdy (2003b). It should also be mentioned that,

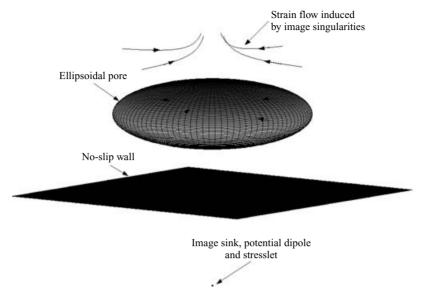


FIGURE 2. A schematic illustrating the idea of the ellipsoidal-pore model. The shrinking pore, assumed to be ellipsoidal at all times, is modelled as existing in a linear straining flow induced by the image singularity distribution associated with a point sink of strength equal to the pore's rate-of-change of volume and situated at the centroid of the pore.

when surface tension is absent, an isolated ellipsoidal inclusion of viscosity $\lambda\mu$ remains ellipsoidal when evolving in an ambient linear flow of a host fluid of viscosity μ (Bilby & Kolbuszewski 1977). Notwithstanding the fact that it has not been established mathematically that an ellipsoidal pore with surface tension remains ellipsoidal under evolution in an ambient linear flow, this assumption of our model is supported by a range of experimental evidence (see Hu & Lips 2003 and references therein).

Indeed, with similar assumptions, Maffettone & Minale (1998) have presented a simple phenomenological model for the transient deformation of an ellipsoidal droplet with capillarity, for small λ , evolving in a linear ambient flow. They write down equations governing the evolution of the second-rank tensor describing the evolving ellipsoidal shape. In our present model, equations similar to these for the case of a constant-pressure compressible ellipsoidal pore would provide the requisite solution of the relevant inner problem and thereby provide the equations required to close the model. A study of the fully three-dimensional model is currently under investigation by the present authors.

As mentioned earlier, the aim of the present paper is to test the model in the planar case. To do this, the predictions of the elliptical-pore model must be compared to the results of full numerical simulations of the full system. There are also several advantages of the planar case which are not afforded by the three-dimensional geometry: first, the assumption that the pores remain elliptical in an ambient linear flow is not an assumption in two dimensions, but is demonstrably true (Crowdy 2003b). The equations governing the inner problem in the model are therefore exact (and not phenomenological as would be the case if using an extension of the three-dimensional model of Maffettone & Minale (1998) to solve the inner problem). Secondly, conformal mapping methods combined with a complex-variable formulation of the problem can be strategically employed to account for the presence of the no-slip surface thereby

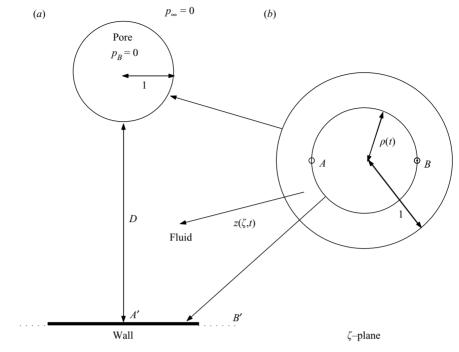


FIGURE 3. (a) A schematic showing a unit-radius circular pore centred at a distance D from an infinite wall at which a no-slip boundary condition is applied. The flow is purely driven by surface tension (so that $p_B = p_\infty = 0$). (b) The conformal mapping pre-image ζ -plane. The annulus $\rho(t) < |\zeta| < 1$ maps to the fluid region above the wall and exterior to the pore. The circle $|\zeta| = 1$ maps to the pore boundary and the circle $|\zeta| = \rho$ maps to the wall. The point A (at $\zeta = -\rho$) maps to the origin A' while the point B (at $\zeta = \rho$) maps to physical infinity B'.

obviating the need to modify the kernels in the usual boundary-integral formulation in a numerical simulation to test the model.

3. Mathematical formulation

Hereinafter, we concentrate on the planar problem and test the predictions of the model with full numerical simulations. This section presents details of the mathematical formulation of the numerical problem in the planar case.

Consider the free surface evolution of a single pore situated some distance above a solid wall lying along the x-axis. Let D be the distance from the wall to the lowest point of the pore boundary. A no-slip condition is applied on the wall. It is assumed that the pressure p_B inside the bubble is a uniform constant, equal to zero at all times. A uniform surface-tension σ acts on the pore boundary. In order that the flow is driven purely by surface-tension effects, the ambient pressure p_{∞} is also be taken equal to zero. Figure 3(a) shows a schematic of the physical flow configuration.

The fluid is assumed to be in the Stokes regime where the Reynolds number is zero, so that

$$-\nabla p + \mu \nabla^2 \mathbf{u} = 0 \tag{3.1}$$

where u = (u, v) is the velocity field, p is the fluid pressure and μ its viscosity. The flow is incompressible so

$$\nabla \cdot \boldsymbol{u} = 0. \tag{3.2}$$

Therefore, a streamfunction $\psi(x, y, t)$ can be introduced with

$$(u, v) = (\psi_v, -\psi_x).$$
 (3.3)

It is easy to show that ψ satisfies the biharmonic equation

$$\nabla^4 \psi = 0 \tag{3.4}$$

everywhere in the fluid. One of the boundary conditions on the bubble is that the tangential fluid stress is zero and that the normal fluid stress component is balanced by the surface tension. This condition on the stress can be written as

$$-pn_i + 2\mu e_{ij}n_j = \sigma \kappa n_i, \tag{3.5}$$

where n_i denotes the *i*th component of the outward-pointing normal vector \mathbf{n} , σ is the surface tension parameter, κ is the surface curvature and e_{ij} is the usual fluid rate-of-strain tensor. There is, in addition, the kinematic condition that the normal velocity of the interface V_n equals the normal fluid velocity, i.e.

$$\boldsymbol{u} \cdot \boldsymbol{n} = V_n. \tag{3.6}$$

Introducing the usual complex coordinates z = x + iy, $\bar{z} = x - iy$, it is known that the general solution of (3.4) can be written

$$\psi(x, y, t) = \text{Im}[\bar{z}f(z, t) + g(z, t)], \tag{3.7}$$

where f(z,t) and g(z,t) are analytic functions in the fluid domain (see Langlois 1964). Straightforward calculations reveal that the physical flow variables are related to these functions via

$$\frac{p}{\mu} - i\omega = 4f'(z, t),
 u + iv = -f(z, t) + z\bar{f}'(\bar{z}, t) + \bar{g}'(\bar{z}, t),
 e_{11} + ie_{12} = z\bar{f}''(\bar{z}, t) + \bar{g}''(\bar{z}, t),$$
(3.8)

where $\omega = -\nabla^2 \psi$ is the vorticity. Conjugate functions, such as $\bar{f}(z)$, are defined by

$$\bar{f}(z) = \overline{f(\bar{z})}. (3.9)$$

It is convenient to non-dimensionalize the problem. If R is some typical length scale of the pore, lengths and times are rescaled with respect to R and $R\mu/\sigma$, velocities with respect to σ/μ and pressure with respect to σ/R .

Using (3.8), the condition of no slip on the wall implies that

$$-f(z,t) + z\bar{f}'(\bar{z},t) + \bar{g}'(\bar{z},t) = 0 \quad \text{on } \bar{z} = z.$$
 (3.10)

It follows that

$$-f(z,t) + z\bar{f}'(z,t) + \bar{g}'(z,t) = 0, (3.11)$$

which is a relation between analytic functions and holds everywhere the functions can be analytically continued. Using (3.8), the stress condition on the pore boundary takes the form

$$\frac{\partial}{\partial s}[f(z,t) + z\bar{f}'(\bar{z},t) + \bar{g}'(\bar{z},t)] = -\frac{1}{2}iz_{ss}.$$
(3.12)

where s denotes arclength around the bubble boundary. Equation (3.12) can clearly be integrated with respect to s to give

$$f(z,t) + z\bar{f}'(\bar{z},t) + \bar{g}'(\bar{z},t) = -\frac{1}{2}iz_s + A(t),$$
 (3.13)

where A(t) is some function of time. An additive degree of freedom in the definition of f(z,t) and g'(z,t) allows us to take A(t) = 0 without loss of generality.

3.1. Symmetries

The pore shape and the associated flow field will be taken to be reflectionally symmetric about the imaginary axis. This means that

$$u + iv|_{-\bar{z}} = -\overline{(u + iv)|_z}.$$
 (3.14)

Using (3.8), it is seen that this implies

$$f(-\bar{z},t) = -\overline{f(z,t)}, \quad \bar{g}'(-z,t) = -\overline{\bar{g}'(\bar{z},t)}, \tag{3.15}$$

or

$$f(-z,t) = -\bar{f}(z,t), \quad g'(-z,t) = -\bar{g}'(z,t).$$
 (3.16)

From (3.11), it follows that

$$\bar{g}'(\bar{z},t) = f(\bar{z},t) - \bar{z}\bar{f}'(\bar{z},t), \tag{3.17}$$

which can be substituted into (3.13) to yield

$$f(z,t) + f(\bar{z},t) + (z-\bar{z})\bar{f}'(\bar{z},t) = -\frac{1}{2}iz_s$$
 (3.18)

on the pore boundary. Equation (3.18) must be solved for f(z, t).

3.2. Conformal mapping

To solve (3.18), introduce a conformal map $z(\zeta,t)$ from an annulus $\rho(t) < |\zeta| < 1$ to the fluid domain. Such a mapping exists, for some choice of $\rho(t)$ which must be found as part of the solution, by the Riemann mapping theorem. Let the circle $|\zeta| = \rho(t)$ map to the wall and let $|\zeta| = 1$ map to the pore boundary. The point $\zeta = \rho$ will be supposed to map to infinity so that $z(\zeta,t)$ has a simple pole at this point. The point $\zeta = -\rho$ will map to z = 0. Figure 3(b) shows a schematic of the mapping regions.

Let z_a denote some point on the wall and let ζ_a be the point on the circle $|\zeta| = \rho$ mapping to z_a . Then,

$$z_a = z(\zeta_a, t). \tag{3.19}$$

By symmetry, we expect the point $\bar{\zeta}_a$ which is also on the $|\zeta| = \rho$ circle to map to $-z_a$, i.e.

$$-z_a = z(\bar{\zeta}_a, t). \tag{3.20}$$

Combining (3.19) and (3.20) implies

$$z(\rho^2 \zeta^{-1}, t) = -z(\zeta, t),$$
 (3.21)

where we have used the fact that $\bar{\zeta} = \rho^2 \zeta^{-1}$ on $|\zeta| = \rho$. Taking the conjugate of (3.20) implies

$$-z_a = \bar{z}(\zeta_a, t), \tag{3.22}$$

from which we deduce, comparing (3.22) and (3.19), that

$$\bar{z}(\zeta, t) = -z(\zeta, t). \tag{3.23}$$

Now let

$$z(\zeta,t) = \frac{\mathrm{i}a(t)}{\zeta - \rho(t)} + \hat{z}(\zeta,t) \tag{3.24}$$

for some real function a(t) and let $\hat{z}(\zeta, t)$ have a Laurent expansion

$$\hat{z}(\zeta,t) = i \sum_{n=-\infty}^{\infty} a_n(t) \zeta^n, \qquad (3.25)$$

convergent for $\rho < |\zeta| < 1$. Define also the functions $\mathcal{F}(\zeta, t)$, $\mathcal{G}(\zeta, t)$ and $\mathcal{H}(\zeta, t)$ as follows:

$$\mathcal{F}(\zeta,t) \equiv f(z(\zeta,t),t),
\mathcal{G}(\zeta,t) \equiv g'(z(\zeta,t),t),
\mathcal{H}(\zeta,t) \equiv f(\bar{z}(\zeta,t),t).$$
(3.26)

It is can be shown from previous arguments that these functions satisfy

$$\overline{\mathscr{F}}(\zeta) = -\mathscr{F}(\zeta), \quad \overline{\mathscr{G}}(\zeta) = -\mathscr{G}(\zeta), \quad \overline{\mathscr{H}}(\zeta) = -\mathscr{H}(\zeta).$$
 (3.27)

Since the pressure at infinity vanishes, $\mathcal{F}(\zeta, t)$, $\mathcal{G}(\zeta, t)$ and $\mathcal{H}(\zeta, t)$ are all analytic in the annulus $\rho < |\zeta| < 1$ and we can therefore write

$$\mathscr{F}(\zeta) = i \sum_{n = -\infty}^{\infty} F_n \zeta^n, \quad \mathscr{G}(\zeta) = i \sum_{n = -\infty}^{\infty} G_n \zeta^n, \quad \mathscr{H}(\zeta) = i \sum_{n = -\infty}^{\infty} H_n \zeta^n, \tag{3.28}$$

where, owing to (3.27), all coefficients are real. It is also important to note that

$$\mathscr{F}(\zeta,t) = f(z(\zeta,t),t) = f(-z(\rho^2\zeta^{-1},t),t) = f(\bar{z}(\rho^2\zeta^{-1},t),t) = \mathscr{H}(\rho^2\zeta^{-1},t).$$
(3.29)

When $|\zeta| = \rho$ then $|\rho^2 \zeta^{-1}| = \rho$ which means that the expansions (3.28) can be used to expand both sides of relation (3.29), thereby implying the following relationship between the coefficients of \mathscr{F} and \mathscr{H} :

$$F_{-n} = H_n \rho^{2n}. (3.30)$$

In terms of these functions, condition (3.18) takes the form

$$\mathscr{F}(\zeta,t) + \mathscr{H}(\zeta,t) + (z(\zeta,t) + z(\zeta^{-1},t)) \frac{\mathscr{F}_{\zeta}(\zeta^{-1},t)}{z_{\zeta}(\zeta^{-1},t)} = \frac{\zeta z_{\zeta}(\zeta,t)}{2|z_{\zeta}(\zeta,t)|}, \tag{3.31}$$

where we have used (3.23), the relation

$$z_s = \frac{i\zeta z_{\zeta}}{|z_{\zeta}|} \quad \text{on } |\zeta| = 1, \tag{3.32}$$

and the fact that

$$\frac{\overline{\mathscr{F}}_{\zeta}(\zeta^{-1},t)}{\overline{z}_{\zeta}(\zeta^{-1},t)} = \frac{\mathscr{F}_{\zeta}(\zeta^{-1},t)}{z_{\zeta}(\zeta^{-1},t)}.$$
(3.33)

The Laurent expansion of (3.31), truncated at $\zeta^{\pm (N/2-1)}$ for some choice of N, yields 2N-1 real equations relating the 4N-2 real coefficients $\{F_n, H_n\}$. The 2N-1 real relations (3.30) are used to eliminate the 2N-1 coefficients H_0 , $\{F_n, H_n | n \le 1\}$ from the latter equations resulting in a consistent system of 2N-1 equations to be solved for F_0 , $\{F_n, H_n | n \ge 1\}$. These can be determined from (3.31) in a numerically stable fashion since the formulation is such that no inverse powers of ρ are ever computed.

3.3. Kinematic condition

It should be noted that, by the above manipulations, the problem has been reduced to solving a single functional equation (3.31) for $\mathcal{F}(\zeta, t)$ valid on the unit ζ -circle. Once $\mathcal{F}(\zeta, t)$ has been found, the kinematic condition can be used to time-advance

the interface. This condition says that the bubble interface must move with the local fluid velocity, i.e.

$$Im[(z_t - (u + iv))\bar{z}_s] = 0. (3.34)$$

Note that (3.34) also embodies the no-slip condition on the solid wall because u + iv is zero there and the wall is fixed. Defining $I(\zeta, t)$ to be

$$I(\zeta,t) \equiv \frac{z_t(\zeta,t)}{\zeta z_{\zeta}(\zeta,t)},\tag{3.35}$$

we can write

$$\operatorname{Re}[I(\zeta,t)] = \begin{cases} \frac{1}{2|z_{\zeta}|} - \operatorname{Re}\left[\frac{2\mathscr{F}(\zeta,t)}{\zeta z_{\zeta}}\right] & \text{on } |\zeta| = 1, \\ -\frac{\dot{\rho}}{\rho} & \text{on } |\zeta| = \rho(t), \end{cases}$$
(3.36)

where we have used (3.32) and the fact that

$$z_s = -\frac{\mathrm{i}\zeta z_\zeta}{\rho |z_r|} \quad \text{on } |\zeta| = \rho(t). \tag{3.37}$$

Overdots denote derivatives with respect to time. It follows from (3.35) that

$$z_t(\zeta, t) = \zeta z_{\zeta}(\zeta, t) I(\zeta, t). \tag{3.38}$$

Once $\mathcal{F}(\zeta, t)$ is determined at each instant, the quantity

$$\frac{1}{2|z_{\zeta}|} + \text{Re}\left[\frac{-2\mathscr{F}(\zeta, t)}{\zeta z_{\zeta}}\right] \equiv \sum_{-\infty}^{\infty} d_{n} \zeta^{n}$$
(3.39)

is also known. Equation (3.39) defines the coefficients $\{d_n\}$. In order that $z_t/\zeta z_\zeta$ is analytic and single-valued for $\rho < |\zeta| < 1$, there is a consistency condition that the constant terms in the Laurent expansions of the right-hand sides of (3.36) on both boundary circles must be equal. That is, we must have

$$-\frac{\dot{\rho}}{\rho} = d_0. \tag{3.40}$$

Equation (3.40) provides an evolution equation for ρ . Defining the Laurent expansion of $I(\zeta, t)$ as

$$I(\zeta, t) = \sum_{-\infty}^{\infty} I_n \zeta^n, \tag{3.41}$$

it follows from (3.36) that

$$I_{0} = d_{0},$$

$$I_{n} = \frac{2d_{n}}{1 - \rho^{2n}} \quad (n \ge 1),$$

$$I_{-n} = -\rho^{2n} I_{n} \quad (n \le 1),$$
(3.42)

which allows $I(\zeta, t)$ to be computed in a numerically stable fashion. Differentiating (3.24) and substituting into (3.38) yields

$$\hat{z}_t(\zeta, t) = \zeta z_\zeta I(\zeta, t) - \frac{\mathrm{i}\dot{a}}{\zeta - \rho} - \frac{\mathrm{i}a\dot{\rho}}{(\zeta - \rho)^2}.$$
 (3.43)

Equation (3.43) depends on the (as yet undetermined) \dot{a} , but its projection onto positive powers of ζ does not. Equating coefficients of positive powers of ζ in (3.43) therefore yields evolution equations for $\{a_n(t)|n \ge 1\}$. From (3.21), it then follows that

$$a_0 = \frac{a}{2\rho}, \quad a_{-n} = -\rho^{2n} a_n \quad (n \geqslant 1),$$
 (3.44)

which yield equations that can be used to update the negative coefficients $\{a_n(t)|n \le 1\}$ once the positive coefficients $\{a_n(t)|n \ge 1\}$ have been updated. This only leaves a to be determined. Once a is found, a_0 follows from (3.44).

To find a, we consider the area $\mathcal{A}(t)$ of the pore. From (3.11),

$$\mathscr{G}(\zeta,t) = \mathscr{F}(\zeta,t) - z(\zeta,t) \frac{\mathscr{F}_{\zeta}(\zeta,t)}{z_{\zeta}(\zeta,t)}.$$
(3.45)

However, it is known that

$$g'(z,t) \sim \text{constant} + \frac{\dot{\mathcal{A}}}{\pi z} + \cdots$$
 (3.46)

Expanding (3.45) about $\zeta = \rho$, it follows that

$$\frac{\dot{\mathcal{A}}}{\pi} = -\mathrm{i}2a\mathcal{F}_{\zeta}(\rho, t),\tag{3.47}$$

where the right-hand side can be computed from the known solution for $F(\zeta, t)$. $\mathcal{A}(t)$ can therefore be found. The formula

$$\mathscr{A}(t) = -\frac{1}{2i} \oint_{|\zeta|=1} \bar{z}(\zeta^{-1}, t) z_{\zeta}(\zeta, t) d\zeta$$
 (3.48)

then yields a quadratic equation for a which can be solved explicitly.

All Laurent expansion coefficients are computed using fast Fourier transforms taken at order \mathcal{N} where, typically, we take $\mathcal{N}=16N$ to avoid aliasing errors. The order N of the truncation is chosen to suit the problem. In most calculations N=64 is adequate; however, it was found necessary to increase this to N=128 for pores that are close to the wall. The system of ordinary differential equations is solved using an explicit backward Euler method.

4. Results

A useful result due to Hopper (1991) is the following formula for the shrinkage time t_* of an elliptical bubble of area π with ratio of semi-minor to semi-major axes \tilde{m} :

$$t_* = \frac{\pi}{2K((1-\tilde{m})/(1+\tilde{m}))} \left(\sqrt{\tilde{m}} + \frac{1}{\sqrt{\tilde{m}}}\right),\tag{4.1}$$

where K(k) is the complete elliptic integral of the first kind. A circular pore corresponds to $\tilde{m} = 1$ which, using $K(0) = \pi/2$, gives the result $t_* = 2$. A graph of t_* against \tilde{m} is shown in figure 4 and shows how the shrinkage time grows for increasing eccentricity of the isolated ellipse.

4.1. The effect of distance from the wall

Assume now that the initial pore is circular with unit radius so that its area is π . In the following calculations, t_* is the time taken for the pore area to reduce to 0.001. For initially circular pores of fixed area π , t_* will be a function of the distance D of

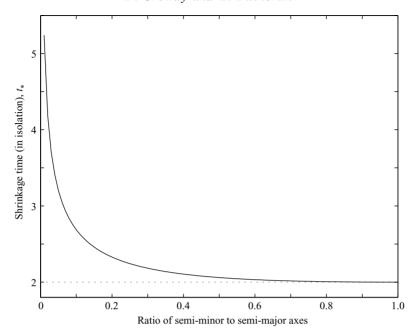


FIGURE 4. Pore shrinkage times t_* for isolated ellipses as a function of \tilde{m} (the ratio of the minor to major axes) as given by (4.1).

the pore from the wall. When the pore is far from the wall, the wall should have little effect so that $t_* \approx 2$ in agreement with Hopper's result (4.1) for an isolated pore.

The initial map must be a Möbius map, since such maps take circles to circles (the real axis is a circle of infinite radius). Indeed, given an initial $\rho(0)$, it is straightforward to show that

$$z(\zeta,0) = i\frac{(1-\rho(0)^2)}{\zeta-\rho(0)} + i\frac{(1-\rho(0)^2)}{2\rho(0)},$$
(4.2)

so that

$$a(0) = 1 - \rho(0)^2$$
, $a_0(0) = \frac{(1 - \rho(0)^2)}{2\rho(0)}$, $a_n(0) = 0$, $n \neq 0$. (4.3)

The distance D between the lowest point of the pore and the wall is found to be

$$D = \frac{(1 - \rho(0))^2}{2\rho(0)}. (4.4)$$

Figure 5 shows calculations for $\rho(0) = 0.2$, 0.5 and 0.8. As expected, when the pore is far from the wall (e.g. for $\rho(0) = 0.2$) it shrinks under the effects of surface tension via a sequence of near-circular shapes with $t_* \approx 2$. This also provides a check on the numerical code. For pores closer to the wall, the shrinkage becomes more anisotropic with the intermediate shapes being no longer circular, but becoming elongated in the y-direction as they become smaller in size. A drift of the centroid of the pore towards the wall is also observed. The portion of the free surface closest to the wall is found to move significantly less than other parts of the boundary, especially when $\rho(0) = 0.8$.

Figure 6 shows a graph of t_* as a function of the initial distance D of the pore from the wall as computed from the simulations. As $D \to \infty$, $t_* \to 2$ while as $D \to 0$,

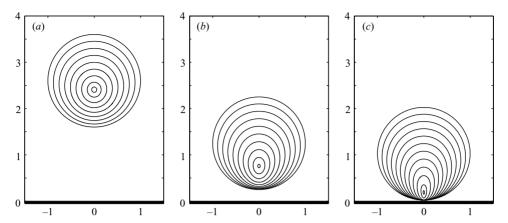


FIGURE 5. Shrinkage of initially circular pores, of initial area π , at various distances from the wall. (a) $\rho = 0.2$, D = 1.6, $t_* = 1.99$; (b) 0.5, 0.25, 2.26; (c) 0.8, 0.025, 2.66. A pore far from the wall shrinks via a sequence of near-circles in time $t_* \approx 2$. Pores very close to the wall shrink in an anisotropic fashion in significantly longer times $t_* \approx 2.66$, the region of the free surface nearest to the wall only moving significantly once the pore has shrunk sufficiently.

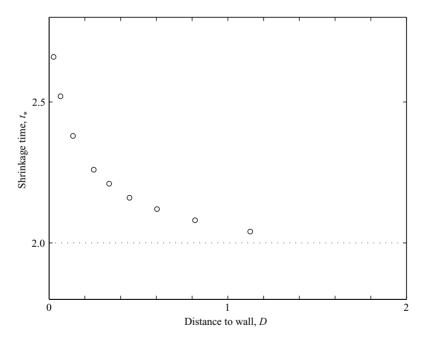


FIGURE 6. Pore shrinkage times t_* as a function of distance D of the initial pore from the wall. When $D \to \infty$, the shrinkage times asymptote to 2. The shrinkage times for pores very close to the wall are found to be about 35 % larger than for pores in isolation.

 t_* increases significantly. An important result is that pores very close to the wall have shrinkage times $t_* \approx 2.66$ so that the effect of the wall is to increase shrinkage times by around 35%. This increase in t_* is observed for $\rho(0) = 0.8$ when the pore starts off at a distance of just 0.025 from the wall.

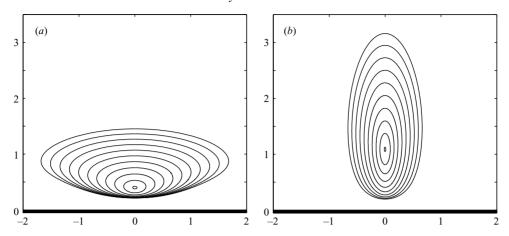


FIGURE 7. Shrinkage of initial ellipse-like bubble of area π and initial aspect ratios approximately (a) 1/3 and (b) 3. Both pores are roughly the same distance from the wall initially. (a) t = 0, (0.25), 2.50; (b) t = 0, (0.25), 2, 2.30.

4.2. The effect of anisotropy of the bubble

The previous calculations take the pores to be initially circular. It is of interest to examine what effect any anisotropy in the bubble shape might have on the pore shrinkage times. It is reasonable to suppose that pores with larger portions of its free surface close to the wall might take longer to shrink to zero area.

To examine this quantitatively, initial ellipse-like configurations with \tilde{m} approximately 1/3 were used as initial conditions in the numerical procedure. The initial conformal maps do not produce shapes that are exactly ellipses: the initial maps were taken from a separate numerical code written to calculate the evolution of two constant-area bubbles in straining flows (see Crowdy, Tanveer & Vasconcelos 2005). The two initial conditions used here were produced by taking two initially circular bubbles and exposing them to strains aligned either along the x or y axes.

Figure 7 shows the results of two simulations, one where the semi-major axis is parallel to the wall (figure 7a), another where the semi-minor axis is parallel to it (figure 7b). Both initial pores have area π and are initially approximately the same distance $D \approx 0.25$ from the wall. A comparison of their respective shrinkage rates should therefore give an indication of the effect of anisotropy on the pore shrinkage rates.

Using Hopper's result (4.1) with $\tilde{m} = 1/3$ gives $t_* = 2.15$ (correct to two decimal places). This is the time taken for an isolated elliptical pore with $\tilde{m} = 1/3$ to disappear. Recall from figure 5 that, even in the case of an isolated pore, the shrinkage time of an elliptical pore increases with \tilde{m} . It is important to bear this in mind when assessing the effects of the wall in what follows.

First, we note that an initially circular pore of area π at the same initial distance $D \approx 0.25$ from the wall has a shrinkage time $t_* \approx 2.25$ which is about 12 % larger than its shrinkage time when in isolation. When the ellipse has a small aspect ratio (so that its semi-major axis is parallel to the wall) it is found that $t_* = 2.54$ (see figure 7). It is again found that the centroid of the pore drifts towards the wall as it shrinks and that the pore becomes stretched in the y-direction. In this configuration, the anisotropy of the bubble in the x and y directions means that a significant portion of the initial free surface is close to the no-slip surface and hence its free motion is impeded. This has the effect of decelerating the global shrinkage rates and leads to an increase of

about 18 % in t_* (compared to the isolated value of 2.15). On the other hand, when the minor axis of the ellipse is parallel to the wall the shrinkage time $t_* = 2.30$ is again larger than the shrinkage time in isolation, but the overall effect of the wall is smaller. In this case, t_* increases (compared to the isolated case) by only 7 %. It is clear that the orientation of an elliptical pore relative to the wall can have significant effects on the shrinkage times. Again, there is a drift of the centroid of the bubble towards the wall and a gradual elongation of the bubble in the vertical direction.

5. The elliptical-pore model

A general feature of the previous calculations is that, as the pores shrink, they become gradually elongated in the y-direction with their centroids moving towards the wall. We now write down the equations of the elliptical-pore model and examine whether these model equations can help to understand this general behaviour.

Consider first the outer flow problem. Suppose a sink, of strength m(t), is at a point ic(t) above a solid wall along the real axis. Then, near ic(t), g'(z, t) has a simple pole, i.e.

$$g'(z,t) \sim \frac{m(t)}{2\pi(z - ic(t))} + O(1).$$
 (5.1)

However, the velocity vanishes on the real axis (where $\bar{z} = z$) so that

$$-f(z,t) + z\bar{f}'(z,t) + \bar{g}'(z,t) = 0.$$
 (5.2)

This relation between analytic functions can be continued off the real axis. Rearranging and taking the complex conjugate yields

$$g'(z,t) = \bar{f}(z,t) - zf'(z,t). \tag{5.3}$$

Now, since g'(z, t) has a simple pole at z = ic(t) and since f'(z, t) must be analytic there, it follows from (5.3) that the conjugate function $\bar{f}(z, t)$ must have a simple pole at z = ic(t). Thus, we pose that

$$\bar{f}(z,t) = \frac{m(t)}{2\pi(z - ic(t))}.$$
 (5.4)

This means that

$$f(z,t) = \frac{m(t)}{2\pi(z + ic(t))}. (5.5)$$

Substituting into (5.3) and rearranging gives

$$g'(z,t) = \frac{m(t)}{2\pi(z - ic(t))} + \frac{m(t)}{2\pi(z + ic(t))} - \frac{ic(t)m(t)}{2\pi(z + ic(t))^2}.$$
 (5.6)

Thus, we have derived the image singularity system for a point sink near a wall: the first term on the right hand side of (5.6) is the point sink, the second term is an equal point sink at the reflected point in the wall (i.e. z = -ic(t)) while the third term represents a potential dipole, with vertical orientation, at the same image point. Note also from (5.5) that the simple pole in f(z,t) at the reflected point corresponds to an image stresslet. In total, the image system for a point sink near a wall consists of a superposition of three image singularities at the reflected point: a sink, a potential dipole and a stresslet. Blake & Chwang (1974) derived a similar image distribution in the three-dimensional case. Figure 8 shows a schematic of the streamlines associated with this outer flow solution and highlights the asymmetry of these streamlines with respect to reflection in the wall.

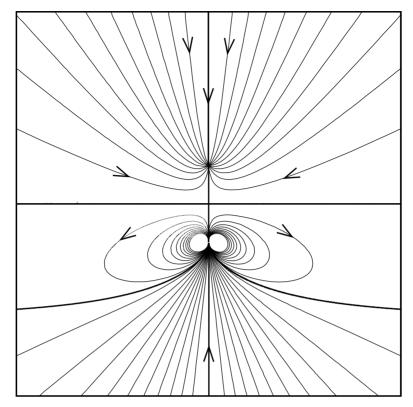


FIGURE 8. Streamlines associated with a sink situated near a wall. The upper half of the diagram shows the physical streamlines. While they are non-physical, the 'image streamlines' are also shown in the lower half of the diagram. The bold curve is the contour $\psi = 0$. This is the 'outer' flow solution in the elliptical-pore model.

With this solution to hand, the 'outer' velocity field

$$u - iv = -\bar{f}(\bar{z}, t) + \bar{z}f'(z, t) + g'(z, t)$$
(5.7)

can be expanded about the centroid ic(t) of the elliptical pore. Letting

$$z = ic(t) + \mathcal{Z}, \quad \bar{z} = -ic(t) + \overline{\mathcal{Z}},$$
 (5.8)

substituting into (5.7) and expanding to linear order in \mathscr{Z} and $\overline{\mathscr{Z}}$ yields

$$u - iv = \frac{m}{2\pi \mathscr{Z}} - \frac{im}{2\pi c} + \frac{m}{8\pi c^2} \mathscr{Z} + \dots$$
 (5.9)

There is no linear term in $\overline{\mathcal{Z}}$ so there is no vorticity in the far field for the inner problem. Already, the model predicts the qualitative features of the preceding numerical simulations. The first term on the right-hand side of (5.9) is the point sink (we expect m(t) to be negative for a shrinking pore). The second term corresponds to a net velocity of the centroid. Indeed, we immediately deduce

$$\dot{c} = \frac{m}{2\pi c}.\tag{5.10}$$

Since m < 0 and c > 0, (5.10) shows that the centroid of the pore moves towards the wall. The third term on the right-hand side of (5.9) corresponds to an irrotational

far-field straining flow where, since m < 0, there is positive strain in the the y-direction. This explains why the pores become elongated vertically.

The inner problem is to solve for the evolution of an ellipse, with centroid at ic(t) and a far-field ambient straining flow

$$u - iv \sim \frac{m}{8\pi c^2} \mathscr{Z}. \tag{5.11}$$

To describe the evolution of the pore shape, introduce a conformal map from the interior of the unit circle in a complex η -plane to the fluid region exterior to the elliptical pore. The map has the form

$$\mathscr{Z}(\eta, t) = \mathrm{i}c(t) + \frac{\alpha(t)}{\eta} + \beta(t)\eta. \tag{5.12}$$

The evolution equations for $\alpha(t)$ and $\beta(t)$ are given in (3.17) and (3.18) of Crowdy (2003b). They are

$$\begin{aligned}
\dot{\alpha} &= -\alpha I(0, \alpha, \beta), \\
\dot{\beta} &= -\beta I(0, \alpha, \beta) + 2k(t)\alpha,
\end{aligned} (5.13)$$

with

$$k(t) = \frac{m}{8\pi c^2} \tag{5.14}$$

and

$$I(0,\alpha,\beta) = \frac{1}{4\pi} \oint_{|\eta|=1} \frac{\mathrm{d}\eta}{\eta} \frac{1}{|\mathscr{Z}_{\eta}(\eta,t)|}.$$
 (5.15)

Moreover, since the area of the ellipse is $\pi(\alpha^2 - \beta^2)$, it follows that

$$m = 2\pi(\alpha\dot{\alpha} - \beta\dot{\beta}). \tag{5.16}$$

From (5.10) and (5.16),

$$c\dot{c} = \alpha \dot{\alpha} - \beta \dot{\beta},\tag{5.17}$$

which can be integrated to yield

$$c^2 = \alpha^2 - \beta^2 + c_1, \tag{5.18}$$

where c_1 is a constant. For initially circular pores,

$$\alpha(0) = 1, \quad \beta(0) = 0, \quad c(0) = \frac{1 + \rho(0)^2}{2\rho(0)},$$
 (5.19)

which yields

$$c_1 = \frac{(1 - \rho(0)^2)^2}{4\rho(0)^2}. (5.20)$$

Furthermore, substituting (5.14) and (5.16) into (5.13) and rearranging, yields the final form of the equations governing the model system:

$$\dot{\alpha} = -\alpha I(0, \alpha, \beta),
\dot{\beta} = -I(0, \alpha, \beta) \left(\frac{2\alpha^2 \beta - 2\beta^3 + 2c_1 \beta + \alpha^3}{2\alpha^2 - 2\beta^2 + 2c_1 + \alpha\beta} \right),
c = \sqrt{\alpha^2 - \beta^2 + c_1}.$$
(5.21)

Note that the model incorporates both surface-tension effects and interaction effects with the wall.

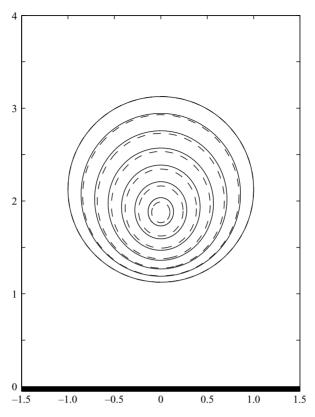


FIGURE 9. Comparison of evolution, for an initially circular pore with $\rho(0) = 0.25$, as given by the analytical model (dashed lines) and the full numerical simulation (solid lines). D = 1.125. Times shown are t = 0, (0.25), 1.75.

As well as providing an explanation for the general qualitative behaviour seen in the numerical simulations, the model may also provide quantitative predictions for pores that are sufficiently far from the wall. To examine this, figure 9 shows a superposition of the results of a full numerical simulation and the results of the model for the choice $\rho(0) = 0.25$. For these initial conditions, the distance of the pore from the wall is D = 1.125. This is not so close to the wall as to invalidate the model, but not so far that wall effects will be negligible. The model is found to give reasonably good agreement to the pore shape evolution although the agreement between the pore shapes seems to deterioriate as time progresses. The model is found to provide good estimates for the evolution of the pore centroid, and slightly underpredicts the pore shrinkage time, yielding a value $t_* \approx 2.0$ while the full numerical simulation yields $t_* = 2.04$. For larger values of $\rho(0)$ (so that the distance of the pore from the wall decreases) the accuracy of the model deteriorates as expected since the separation between inner and outer length scales (on which the model depends) is no longer well-defined.

6. Discussion

The comparison of full numerical simulations with the predictions of the ellipticalpore model gives convincing evidence of the viability of the model in the planar case. These results provide strong motivation for formulating the analogous 'ellipsoidal-pore' model in the three-dimensional case (as described in §2) and work in this direction is currently in progress. As mentioned in §1, the inspiration for the present model was the 'elliptical-vortex approximation' of two-dimensional vortex dynamics. The natural generalization of this planar model to an 'ellipsoidal-vortex model' has been implemented by the vortex dynamics community (see Dritschel, Reinaud & McKiver 2004).

If the pore is elongated in a particular direction (so that it is far from spherical), the assumption that the pore is well-modelled by a point sink at its centroid must be expected to become a poor approximation. However, in such circumstances, it is worth mentioning another possible avenue for the incorporation of three-dimensional effects and hence a possible extension of our model. This is relevant to the particular case of slender pores where recent work by Howell & Siegel (2005) has demonstrated that when such pores evolve in an ambient straining flow they can be analysed, under a slender-body approximation, as a sequence of weakly coupled two-dimensional problems within the same complex-variable formulation as considered here. Thus, we can envisage modelling the shrinkage of slender three-dimensional pores near a wall as a sequence of weakly coupled 'elliptical-pore' model equations (as presented here), the straining flow in which this slender pore finds itself being generated by a line of image singularities in the wall (i.e., a continuous line of singularities in contrast to a point singularity). The viability of this idea is under investigation. Note also that the case of long slender bubbles is particularly interesting because one expects the effects of hoop stress to become significant in this geometrical configuration. A dominant hoop stress may lead to break-up of the pore and consequently the formation of multiple pores. Howell & Siegel (2005) find situations within their approximation in which an ambient straining flow can lead to bubble pinch-off.

To summarize the qualitative results, it has been observed that, even before accounting for contact-line effects between the pore interface and the wall, the proximity of a pore to a no-slip surface, as might arise in the viscous sintering of an amorphous matrix containing a distribution of non-densifying rigid platelets, can lead to significant increases in pore shrinkage times. This increase is a combination of two effects: the proximity of the pore to the no-slip surface and the orientation of an anisotropic pore relative to the wall. To summarize our findings, if a pore is near a no-slip surface its shrinkage time t_{*} will generally increase. Increases of up to 35% have been found in the case of isotropic circular pores. Even in isolation, anisotropy in the pores generally leads to an increase in the shrinkage time compared to a circular pore of the same area. When an anisotropic pore is placed near to a wall, the shrinkage times are further increased compared to the same pore in isolation, the overall effect of the wall being greatest when the orientation of the pore relative to the wall is such that a large surface area of the interface is exposed to the wall. At the same time, wall effects for a pore at a given distance from the wall can be decreased by orienting a pore such that it has minimal exposure to the wall.

Intuitively, the presence of the no-slip surface inhibits flow between the wall and the free surface exposed to it, thereby reducing the effects of surface tension in this vicinity. Figure 5 clearly indicates that, in the early stages of the evolution, points on the bubble surface closest to the wall appear to be 'pinned' compared to other regions of the interface. Thus, the surface of the pore nearest to the wall cannot shrink as easily as the region of the pore boundary farthest from the wall. This helps to explain the net displacement of the bubble centroid towards the wall. It also helps to understand the net elongation of the pore in the direction perpendicular to

the wall. What the simulations show in all cases is the gradual 'de-pinning' of the interface nearest to the wall by a process of pore elongation perpendicular to the wall. This elongation increases the local interface curvature in the region closest to the wall leading, in turn, to an increased surface-tension force which causes fluid to be drawn in faster and eventually counters the effect of the no-slip boundary. It should be noted that we expect that qualitatively similar behaviour will be observed in the fully three-dimensional case of, say, a spherical pore near a wall.

A question arising from figure 6 is whether $t_* \to \infty$ as $D \to 0$ or whether t_* tends to some finite value. If D is arbitrarily small, but not zero, the general arguments above on the 'de-pinning' mechanism suggest that, for initially circular pores, t_* will tend to some (possibly) large but finite value. The case of D being exactly zero is not captured by our formulation here since then the issue of contact between a free surface and a solid surface must come into play, along with all the concomitant complications associated with contact lines. This is beyond the scope of the present investigation.

The numerical method used here can be extended in various directions. A variant of it has already been used to study the behaviour of two interacting bubbles in an ambient straining flow (Crowdy et al. 2005). It can similarly be adapted to study layers of slow viscous fluid attached to walls (cf Pozrikidis 1988) as well as situations where additional physical effects such as gravity and pore compressibility are included. It can be modified to include contact-line effects between the pore interface and the wall, and this is the subject of on-going work. On the other hand, the method devised here is not extendible to the fully three-dimensional case and alternative schemes such as level-set methods or phase-field methods would be required to tackle this case.

This work is supported by a grant from EPSRC in the UK. The authors are grateful to the anonymous referees for valuable comments and suggestions.

REFERENCES

- Antanovskii L. K. 1994 Quasi-steady deformation of a two-dimensional bubble placed within a potential flow. *Meccanica-J Ital. Assoc. Theor. Appl. Mech.* **29**, 27–42.
- BILBY, B. A. & KOLBUSZEWSKI, M. L. 1977 The finite deformation of an inhomogeneity in twodimensional slow viscous incompressible flow. *Proc. R. Soc.* A **355**, 335–353.
- BLAKE, J. R. & CHWANG, A. T. 1974 Fundamental singularities of viscous flow. J. Engng Maths 8, 23–29.
- BOCCACCINI, A. R. & CONRADT, R. 2001 Isotropic shrinkage of platelet containing glass powder compacts during isothermal sintering. *Intl J. Inorg. Mat.* 3, 101–106.
- Brinker, C. J. & Scherer, G. W. 1990 Sol-Gel Science: the Physics and Chemistry of Sol-Gel Processing. Academic.
- CHWANG, A. T. & Wu T. Y.-T. 1975 Hydromechanics of low-Reynolds-number flow. Part 2. Singularity methods for Stokes flows. *J. Fluid Mech.* 67, 787–815.
- Crowdy, D. G. 2003a Viscous sintering of unimodal and bimodal cylindrical packings with shrinking pores. *Eur. J. Appl. Maths* **14**, 421–445.
- Crowdy, D. G. 2003b Compressible bubbles in Stokes flows. J. Fluid Mech. 476, 345–356.
- Crowdy, D. G. 2004 An elliptical-pore model of late-stage planar viscous sintering. *J. Fluid Mech.* **501**, 251–277.
- Crowdy, D. G., Tanveer, S. & Vasconcelos, G. L. 2005 On a pair of bubbles in planar Stokes flow. *J. Fluid Mech.* (to appear).
- Dritschel, D. G., Reinaud, J. N. & McKiver, W. J. 2004 The quasi-geostrophic ellipsoidal vortex model. *J. Fluid Mech.* **505**, 201–223.
- Greengard, L., Kropinksi, M. C. & Mayo, A. 1996 Integral equation methods for Stokes flow and isotropic elasticity in the plane. *J. Comput. Phys.* 125, 403–414.

- HOPPER, R. W. 1990 Plane Stokes flow driven by capillarity on a free surface. *J. Fluid Mech.* 213, 349–375.
- HOPPER, R. W. 1991 Plane Stokes flow driven by capillarity on a free surface. J. Fluid Mech. 230, 355-364.
- Howell, P. D. & Siegel, M. 2005 The evolution of a slender non-axisymmetric drop in an extensional flow. *J. Fluid Mech.* **521**, 155–180.
- Hu, Y. T. & Lips, A. 2003 Transient and steady-state three-dimensional drop shapes and dimensions under planar extensional flow. *J. Rheol.* 47, 349–369.
- Kuiken, H. K. 1990 Viscous sintering: the surface-tension-driven flow of a liquid form under the influence of curvature gradients at its surface. *J. Fluid Mech.* **214**, 503–515.
- LANGLOIS, W. E. 1964 Slow viscous flow, Macmillan.
- MAFFETTONE, P. L. & MINALE, M. 1998 Equation of change for ellipsoidal drops in viscous flow. J. Non-Newtonian Fluid Mech. 78, 227–241.
- MELANDER, M. V., ZABUSKY, N. J. & STYCZEK, A. J. 1986 A moment model for vortex interactions of the two-dimensional Euler equations. Part 1. Computational validation of a Hamiltonian elliptical representation. *J. Fluid Mech.* 167, 95–115.
- MIKHLIN, S. G. 1957 Integral equations Pergamon.
- POZRIKIDIS C. 1988 The flow of a liquid film along a periodic wall. J. Fluid Mech. 188, 275-300.
- POZRIKIDIS, C. 1992 Boundary integral and singularity methods for linearized viscous flow, Cambridge University Press.
- POZRIKIDIS, C. 2000 Expansion of a compressible bubble in Stokes flow. J. Fluid Mech. 442, 171–189.
- POZRIKIDIS, C. 2003 Computation of the pressure inside bubbles and pores in Stokes flow. *J. Fluid Mech.* 474, 319–337.
- RICHARDSON, S. 2000 Plane Stokes flow with time-dependent free boundaries in which the fluid occupies a doubly-connected region. *Eur. J. Appl. Math.* 11, 249–269.
- SAFFMAN, P. G. 1992 Vortex dynamics. Cambridge University Press.
- SCHERER, G. W. 1987 Sintering with rigid inclusions. J. Am. Ceram. Soc. 70, 719–725.
- Tanveer, S. & Vasconcelos, G. L. 1995 Time-evolving bubbles in two-dimensional Stokes flow *J. Fluid Mech.* 301, 325–344.
- Van de Vorst, G. A. L 1993 Integral method for a two-dimensional Stokes flow with shrinking holes applied to viscous sintering. *J. Fluid Mech.* **257**, 667–689.